Type II porous ionic liquid based on metal-organic cage that enables L-tryptophan identification

Zhuxiu Zhang
Nanjing Tech University
Baolin Yang
Nanjing Tech University
Bingjie Zhang
Nanjing Tech University
Mifen Cui
Nanjing Tech University
Jihai Tang (jhtang@njtech.edu.cn)
Nanjing Tech University
Xu Qiao
Nanjing Tech University

Article

Keywords: HD/THTP_Cl, L-Trp, Type-II porous ionic liquid

Posted Date: November 15th, 2021

DOI: https://doi.org/10.21203/rs.3.rs-1019974/v1

Abstract

Porous liquids with chemical separation properties are quite well-studied in general, but there is only a handful of reports in the context of identification and separation of non-gaseous molecules. Herein, we report the first example of Type-II porous ionic liquid that exhibits exceptional selectivity towards L-tryptophan (L-Trp) over other aromatic amino acids and the first in which coordination cages promote this selectivity. A previously known class of anionic organic-inorganic hybrid doughnut-like cage (HD) has been readily dissolved in trihexyltetradecylphosphonium chloride (THTP_Cl). The resulting liquid, HD/THTP_Cl, is thereby composed of common components, facile to prepare, and exhibit room temperature fluidity. The permanent porosity are manifested by the high-pressure isotherm for CH4 and modeling studies. With evidence from time-dependent amino acid uptake, competitive extraction studies and molecular dynamic simulations, HD/THTP_Cl exhibit better selectivity towards L-Trp than existing solid state sorbents, and we attribute it to not only the intrinsic porosity of HD but also the host-guest interactions between HD and L-Trp. Specifically, each HD unit is binded with nearly 5 L-Trp molecules, which is higher than the L-Trp occupation in the structure unit of other benchmark metal-organic frameworks.

Introduction

Porous liquids represent an emerging class of materials that combine the benefits of porosity and fluid properties in a rational manner[1-3]. The intrinsic porosities of porous liquids are mainly derived from components with either zero dimensional nanostructures (e.g. molecular cages[4], hollow silica[5]) or extended network structures (e.g. metal-organic frameworks[6] and zeolites[7]). Their modular nature and structure diversity facilitate the exquisite control over porous liquids with respect to the pore size and chemistry through the judicious selection of structural constituent. Such versatile porosities thereby enable systematic studies that afford an understanding of structure-function relationships of porous liquids, which has led them to be of particular interest for potential utility in gas storage[8-16], separations[17-20] and catalysis[21-23].

More than one third of pore liquids consist of molecular cages including porous organic cages (POCs) and metal-organic cages (MOCs) as pore hosts. Molecular cages are generally solid state materials at atmospheric condition. The functionalization of their periphery with alkyl chains[24,25] or poly(ethylene glycol) chains[4] offers opportunities to reduce the melting point, giving rise to the Type I porous liquids. Another synthetic approach of Type I porous liquids is to transform the anionic POC into ionic liquid by pairing with cationic 18-crown-6/K^+ complex[26]. However, most of molecular cage-derived porous liquids are generated via dissolving molecular cages in bulky solvents, also known as Type II porous liquids. The dissolution process is essentially simpler than multi-step organic synthesis involved in the synthesis of Type I porous liquids.

MOCs[27-29] are an important class of discrete nanoscale structures amenable to crystal engineering[30,31] and can be rationally designed using the 'node-and-spacer' approach. The pre-selection of nodes and spacers enables the fine-tuning of structure and properties, so that MOCs can be regarded as ideal pore hosts for Type II porous liquids. In fact, MOCs have been explored in liquid phase to extract target molecules from another immiscible liquid phase via host-guest binding affinity[32]. There is also a handful of papers regarding the gas encapsulation in cavities of MOCs in solution[33]. However, the use of volatile solvent and the unwanted occupation of the cage cavity fails to endow the solution of MOCs with permanent porosity. To our knowledge, there is only one MOC-based Type-II porous liquid generated by dissolving MOP-18 in 15-crown-5[18]. In this contribution, we introduce a new class of Type II porous liquids composed of anionic organic-inorganic hybrid doughnut-like nanostructures (HD)[34] dissolved in trihexyltetradecylphosphonium chloride (THTP_Cl). Note that it is also the first example of Type-II porous ionic liquid based upon MOCs.

Molecular cages, including those serve as the "doughnut-shaped" host (e.g. cyclodextrin and cucurbiturils), have been of particular interest in the contemporary supramolecular chemistry[35]. Porous liquids consisting of molecular cages thereby exhibit host-guest properties, as exemplified by the shape and size selectivity for a series of isomeric alcohols in Type I porous ionic liquids composed of tetrahedral coordination cage[4]. Most recently, Xia *et al* reported the use of the cyclodextrin-derived Type-I porous liquid for the efficient chiral recognition and separation of nucleosides in the solution[36]. Except for the two examples above, current research on the host-guest properties of the molecular cage-based porous liquids has been mainly focused on the accommodation of small gaseous molecules such as carbon dioxide[8,37,38], methane[11,14,39] and chlorofluorocarbon[4]. It still remains a rare and poorly understood of the capture of non-gaseous guest molecules in porous liquids. The work herein addresses the use of the Type-II porous ionic liquid for the selective extraction of $_L$-Tryptophan ($_L$-Trp) from the aromatic amino acid mixtures in aqueous solution.

Results And Discussion

Synthesis and purification. The crystallization of anionic organic-inorganic hybrid nanodoughnut (HD) with dimethylammonium (DMA) as the counter-ion occurs during the solvothermal reaction of 5-bromo-1,3-benzenedicarboxylatic acid and VCl_3 in DMF. The resulting DMA_HD crystals are difficult to be dissolved in organic solvents (e.g. 15-crown ether and hexachloropropene) that have been used for the synthesis of type II porous liquids, because DMA_HD is essentially a type of salt difficult to be ionic dissociated in the aprotic organic solvent. Fortunately, we observed the readily dissolution of DMA_HD in trihexyltetradecylphosphonium chloride (THTP_Cl) to form the dark green liquid (DMA_HD/THTP_Cl) via stirring at room temperature (Fig. 1a). It's necessary to remove DMA from DMA_HD/THTP_Cl because it may occupy the cavity of HD in the solution. The addition of acetonitrile to DMA_HD/THTP_Cl formed a certain amount of the white precipitate with the melting point (T_m) of 173 °C corresponding to the pure dimethylammonium chloride (Fig. 1b). The bulk purity of the precipitate was furtherly verified by comparing the calculated and experimental X-ray powder diffraction patterns (Fig. 1c). The presence of

methyl group in the white precipitate was determined by ^{1}H-NMR analysis (Fig. 1d). The molar ratio of DMA and HD in DMA_HD/THTP_Cl was determined as 3.85:1 close to the molecular formula of as-synthesized DMA_HD. Therefore, all of DMA cations in DMA_HD/THTP_Cl is almost removed in the form of dimethylammonium chloride, and the only cation in the purified porous liquid (HD/THTP_Cl) is THTP electrically balanced by HD and chloride anion.

Structure characterization. The quadrupole time-of-flight (QTOF) mass spectrum of the HD/THTP_Cl in acetonitrile confirms the existence of HD anion, according to the peaks at the m/z of 853.2508 assigned to the molecular formula of $[(V_4O_8Cl)_4(C_8H_3BrO_4)_8]^{4-}$. Another intense molecular ion peaks at the m/z of 483.5105 is assigned to THTP cation, $[C_{32}H_{68}P]^+$ (Fig. 2a). There are no powder X-ray diffraction peaks of HD/THTP_Cl compared to as-synthesized DMA_HD, excluding the existence of small HD crystallites dispersed in the liquid (Fig. 2b). All HD anions are fully dissolved in the THTP_Cl as indicated by dynamic light scattering measurements with an average size of 1.8 nm, which is in good agreement with diameter of HD cage (Fig. 2c). Thermogravimetric analysis reveals a similar thermal stability between HD/THTP_Cl and THTP_Cl before decomposition (Supplementary Fig. 1). Differential scanning calorimetry (DSC) curves showed an endothermic/exothermic peaks of HD/THTP_Cl and THTP_Cl of −64.42/−70.05 and −68.51/−72.71 °C respectively, corresponding to the melting temperature (T_m) and crystallization temperature (T_c). HD/THTP_Cl and THTP_Cl exhibited a similar thermal hysteresis behavior related to the reversible first-order structural phase transition[40]. Both T_m and T_c of HD/THTP_Cl are slightly higher than those in THTP_Cl, which can be tentatively attributed to inhibition of both chains mobility and vibration of THTP cations by HD anions[41] (Fig. 2d).

The rheological properties of HD/THTP_Cl were studied by a rotational rheometer. The frequency sweeps were conducted within a linear viscoelastic region between 0.1% and 1% from an initial amplitude sweep (Fig 2e inset). The liquid-like behavior is reflected by higher storage modulus (G') than loss modulus (G") at low angular frequency range. The equivalent modulus value indicates the solid-liquid transition of HD/THTP_Cl at an angular frequency of 39 rad/s (Fig. 2e). HD/THTP_Cl shows the evidence of Newtonian fluid as the linear dependence of shear stress on the shear rate (Supplementary Fig. 2). The viscosity of HD/THTP_Cl thereby remain invariant of 0.7 Pa·s with increasing shear rate (Supplementary Fig. 3), and it was even lower than the viscosity of pure THTP_Cl at 25 ℃ (1 Pa·s) (Fig. 2f).

Demonstration of porosity in HD/THTP_Cl. Molecular Dynamics (MD) simulations of a bulk system consisting of 5 HD anions, 400 THTP cations and 96 chloride anions in a cubic and periodic simulation box were carried out in the NPT ensemble at 1 bar and 298 K with a time-step of 2 fs. To estimate the energy barrier for THTP cations and chloride anions transporting through the HD anion, the potential of mean force (PMF) was studied via radial distribution functions. The approaching of THTP cations and chloride anions to HD causes the significant increase of PMF from 0 to 12.5 kJ/mol, so that the minimum distance between HD and chloride anions are at approximately 0.8 nm (Fig. 3a). In contrast, the distance between HD anion and THTP cation can be as close as approximately 0.45 nm, which is consistent with the larger interaction energy of −120 kJ/mol than that of −50 kJ/mol between HD anion and chloride

anion due to electrostatic repulsion (Fig. 3b). On average, around 100% of the THTP cations at any given time are outside the HD anions so that there is enough void cavities in HD/THTP_Cl (Fig. 3c).

The MD simulation result detailed herein prompted us to evaluate the high-pressure CH_4 adsorption ability of HD/THTP_Cl, and THTP_Cl was also chosen as the contrast. The gravimetric CH_4 uptakes (298 K, 65 bar) in HD/THTP_Cl and THTP_Cl are 0.28 and 0.18 mmol/g respectively. The uptake difference between HD/THTP_Cl and THTP_Cl corresponds to an average of four CH_4 molecules adsorbed per HD cage. (Fig. 3d). We then carried out a simulation of the 1:100:96 mixture of HD, THTP and chloride ions combined with 100 methane molecules. The starting configuration was generated by randomly placing 100 methane molecules in the bulk fluid without any atomic overlaps. The system was then relaxed for 10 ns under NPT conditions, and all methane molecules were observed freely flowed in HD/THTP_Cl during the simulations (Fig. 3e). Supplementary Figure 4 shows the number of methane molecules residing in the HD cavity as a function of time during the production run at T=298 K and P = 65 bar. The methane molecule instantly diffuses into the cavity and there are 3~5 methane molecules residing in HD cavity at any one time on average, which is consistent with the experimental result.

Selective extraction of $_L$-tryptophan from aromatic amino acids mixture. $_L$-Tryptophan ($_L$-Trp) is one of the eight essential amino acids that play a key role in human metabolism as exemplified by the biosynthesis of neurotransmitters, hormones, and vitamins. The isolation and purification of $_L$-Trp from the fermentation broth that contains $_L$-tyrosine ($_L$-Tyr) and $_L$-phenylalanine ($_L$-Phe) as major impurities is an important for the $_L$-Trp production. Liquid–liquid extraction is one of the widely used separation methods, and experiments were carried out by allowing 0.1 mL of HD/THTP_Cl come into contact with 2 mL of aqueous solution containing different types of amino acids. For the single component system, Figure 4a presents a significant increase of the extraction rate before equilibrium as indicated by the incremental concentration of $_L$-Trp in the HD/THTP_Cl phase during the timeframe of 1–4 h. The extraction reached equilibrium at 8 h as exhibited by the plateau from kinetic curves, and the final $_L$-Trp uptake was 108.2 μmol/L after 24 h. Comparably, the extraction ability of THTP_Cl was significantly reduced to 17.7 μmol/L over the whole extraction time range. In addition, neither $_L$-Tyr or $_L$-Phe was extracted by HD/THTP_Cl or THTP_Cl after 24 hours (Supplementary Fig. 5-6). The reuse of HD/THTP_Cl were realized by adding ethanol/water solution (1:4) for back extraction, followed by being vacuum dried at 60 ℃ for 2 h. Figure 4b shows that HD/THTP_Cl does not lose its extraction ability after 5 extraction cycles.

To support and confirm the high selectivity derived from the single-component extraction experiments, the selective $_L$-Trp extraction by HD/THTP_Cl from the model solution that contains equimolar mixture of $_L$-Trp, $_L$-Tyr and $_L$-Phe was investigated and presented in Fig. 4c. The initial concentration of each amino acid in water phase is 2 mmol/L with the water:HD/THTP_Cl phase ratio of 20:1, and higher phase ratio means lower initial concentration of amino acids. Both concentrations of $_L$-Tyr and $_L$-Phe are close to zero at phase volume ratio of 80:1, 40:1 and 20:1. The concentration of $_L$-Trp in aqueous phase after extraction is 0.1 mmol/L at the phase volume ratio of 80:1. When the phase volume ratio increase to 20:1,

the corresponding concentration of $_L$-Trp in water after extraction is 1.7 mmol/L. The separation factor is 24 for $_L$-Trp to $_L$-Phe and 23 for $_L$-Trp to $_L$-Tyr at the phase ratio of 20:1, whereas the corresponding separation factor are reduced to 0.94 and 0.93 at the phase ratio of 80:1. These results suggest that $_L$-Trp can be selectively separated from a mixture of amino acids by HD/THTP_Cl, and the use of low phase volume ratios, such as 20:1, is beneficial to the high extraction selectivity.

The high selectivity toward $_L$-Trp exhibited by HD/THTP_Cl is then addressed through molecular dynamic simulations in which amino acid molecules is added in the simulation box for probing the recognition ability of HD. The simulation system containing $_L$-Trp molecules reach stability within 1 ns and remain stable for the rest simulation time. There are one $_L$-Trp molecule encapsulated in the cage of HD and four $_L$-Trp molecules surrounding the periphery of HD cage (Fig 4d and Supplementary Fig. 7-8). In comparison, the more fluctuated higher root mean square deviations (RMSD) value of $_L$-Phe and $_L$-Tyr simulation system were found within 2 ns and 3.5 ns, indicating of highly bias and instability of the simulation systems (Supplementary Fig. 9-11 and Supplementary Table 1). This explain why $_L$-Phe and $_L$-Tyr are not extracted by HD/THTP_Cl. Noncovalent interactions between $_L$-Trp molecule and HD were determined using reduced density gradient (RDG) analysis[42]. The RDG isosurface is colored according to the value of sign(λ_2)ρ to distinguish the different weak interactions, and the type of the interaction is illustrated by the blue-green-red scale (blue: strong absorption including hydrogen bond and strong halogen bond, green: van der Waals interactions, red: steric hindrance) (Supplementary Fig. 12-13). The van der Waals interaction and C–H···π interactions (d[C–centroid$_{phen}$] = 4.2 Å) between the encapsulated $_L$-Trp and HD cage can be clearly detected according to the dispersed low density isosurfaces between $_L$-Trp and the benzene ring of ligand (Supplementary Fig. 14-16). For $_L$-Trp molecules outside the HD cage, the isosurface lies between the nitrogen atom in the indole ring and oxygen atom in the polyoxovanadate, characteristic of weak hydrogen bond (d[N-O] = 2.4 - 3.4 Å) (Supplementary Fig. 17-20). RDG analysis also demonstrates that van der Waals interaction play important roles in the absorption of $_L$-Trp by the periphery of HD cages (Supplementary Fig. 13).

As with the experimental and modelling results discussed above, $_L$-Trp molecules were not only encapsulated in almost all of the internal cavities of HD/THTP_Cl, but also interacting with the periphery of HD. The number of $_L$-Trp loaded per HD cage unit was calculated to be 4.7. Although the gravimetrical uptake of $_L$-Trp in HD/THTP_Cl is moderate by the standard of porous materials[43], the unit occupation of HD/THTP_Cl is unprecedented, outperforming other benchmark porous coordination polymers: 1.3 for UIO-66, 0.4 for MIL-140B, 2.1 for MIL-140C, 1.5 for MIL-140D, 2.2 for MOF-808, 2.6 for MIL-68(Al) and 2.7 for zeolite HY calculated via dividing the gravimetric uptake of $_L$-Trp by the molecular weight contained in one unit cell of certain MOF (Fig. 4e). The low unit occupation by $_L$-Trp observed in these porous coordination polymers may originate from two factors: (i) limited access of the $_L$-Trp in narrow pore environment. Adsorbents such as UiO-66 have narrow channel (5 to 11 Å) that are comparable of the $_L$-Trp dimension (11.1×6.4×8.1 Å) calculated by Multiwfn program[44], so that the penetration of the $_L$-Trp

might be restricted; (ii) restricted diffusion of the $_L$-Trp to the inner structure. The growth of the MOF or zeolite crystalline particle inevitably resulted in the significant mass transfer resistance since the large particles have a prolonged internal diffusion pathway, thus providing barrier for the penetration of the adsorbate to deeper into the adsorbent structure[45]. In contrast, HD cages are readily accessible to $_L$-Trp, so that there is no side effect of internal diffusion in HD because it is the zero-dimensional structures highly dispersed in the THTP_Cl.

In summary, HD/THTP_Cl is only the third example of porous liquid that exhibits a non-gaseous guest molecules selectivity and the first type-II porous ionic liquid based upon coordination cages that induce such selectivity. The modeling and several experimental studies provide structural insight into the existence of the permanent porosity in THTP_Cl with 6% HD. Compare with pure THTP_Cl, we have demonstrated how the empty cavity of HD, coupled with favorable host-guest interactions provided by the internal chemical environment of HD cage, affords HD/THTP_Cl with exceptional selectivity and recyclability in the context of industrially relevant $_L$-Trp separation applications. Furthermore, the unit occupation by $_L$-Trp in HD/THTP_Cl is much higher than other benchmark solid state porous material thanks to the pore size and dispersion of HD that enhance the diffusion of the $_L$-Trp molecules into the intrinsic pores of HD/THTP_Cl. Perhaps most importantly, HD belongs to one of the most extensively studied and broadest classes of polyoxovanadate-based coordination cages[46] and is therefore likely to serve as prototypal to promote a platform of related porous liquid with potential to resolve industrial challenges related to molecular separation.

Methods

Synthesis of HD/THTP_Cl. All reagents and solvents were purchased from commercial sources and used without further purification. The HD (0.36 g, 0.1 mmol, 1.0 eq.) was added in THTP_Cl (5.19 g, 10 mmol, 100.0 eq.). The obtained mixtures were vigorously stirred at room temperature. The resulting green solution was added 5 mL acetonitrile and centrifuged to remove the precipitation. Finally, a green liquid was collected after rotary evaporation to remove acetonitrile.

Structure analysis. Powder x-ray diffraction (PXRD) patterns of the samples were collected at 40 kV and 40 mA on a Rigaku SmartLab diffractometer with Cu Kα (λ = 1.5416 Å) radiation with 10°/min scan speed of and 0.02° in 2θ step size. ^{1}H NMR spectrum was obtained on a Bruker 400 MHz spectrometer using D_2O as solvent. Mass spectrum was obtained using an Agilent 6530 Q-TOF mass spectrometer in positive-ion detection mode. Dynamic Light Scattering (DLS) measurements were performed using a Zetasizer Nano ZS90 under 2 min thermal equilibrium. Elemental analysis was performed on elementar vario EL cube. Cl content was obtained by potentiometric titration through argentometric method applied automatic potentiometric titrator (LEICI ZDL-4B). High-pressure CH_4 adsorption data were collected using

a gravimetric sorption analyzers-isoSORP®, from Rubotherm-TA instrument at 25 ℃ and a pressure range of 0-65 bar.

Thermal analysis. Thermal gravimetric analysis (TGA) was performed on Mettler Toledo TGA/DSC from 25 ºC to 650 ºC at 10 °C/min under N_2 with a flow rate of 40 mL/min. Differential scanning calorimetry (DSC) measurements were taken under N_2 atmosphere in the temperature range from -85 to 80℃ at a heating rate of 10 ℃/min by using the DSC Q-20 TA instrument. To remove the thermal history, samples were precooled from 25 to -85 ℃, then reheated from -85 to 80 ℃ to collect data.

Rheologic analysis. Rheological properties were studied using Anton Paar MCR302. Strain -dependent and frequency-dependent rheology measurements were test by equipping CP25-2-SN27479 with a gap of 0.104 mm at room temperature. For temperature-dependent viscosity and stress versus shear rate measurements were test by equipping PP25-SN27504 with a gap of 0.100 mm under rotation mode.

Extraction experiments. Typically, 0.10 mL of HD/THTP_Cl was mixed with 2.0 mL of $_L$-Trp aqueous solution (0.05 mol/L). followed by vigorous stirring for 8 h at room temperature. The amino acid uptake were determined using a Agilent 1260 Infinity II Prime LC system equipped with G1311 Quatpump, G1314F wavelength detector and Agilent ZORBAX SB-C18 column (150 mm × 4.6 mm i.d., 5 μm particles). Amino acids were detected at specific wavelengths: 258 nm for $_L$-Tyr, 280 nm for $_L$- Phe and $_L$-Trp. The mobile phase was composed of potassium dihydrogen phosphate aqueous solution (8 mmol/L) and HPLC-grade methanol with volumetric ratio of 9:1. The flow rate was set at 0.5 mL/min. Calibration curve of amino acid were presented in Supplementary Figures. Extraction experiments were carried out in triplicate.

The Amino acid separation factor $S_{i/j}$ was calculated according to the equation (1):

$$S_{i/j} = \left(x_i / x_j\right) / \left(y_i / y_j\right) \quad (1)$$

where x is the mole fraction in HD/THTP_Cl phase, y is the mole fraction in the aqueous phase at equilibrium, i represents $_L$-Trp, and j represents any other amino acid, respectively.

Structure unit occupation was calculated according to the equation (2):

$$Structure\ unit\ occupation = q_e \times M \quad (2)$$

where q_e is the gravimetric uptake of amino acid (mol/g), M is the molecular weight of one HD unit or the molecular weight contained in one unit cell of MOF (g/mol).

Computational details. All the all-atom MD simulations were based on a gromos54a7 force field[47] by Automated Topology Builder (ATB) [48] and were carried out using the Gromacs-4.6.7 software package[49]. The system is a relaxed liquid configuration at 298 K. The total run time was 10 ns NPT for the equilibrium MD simulation. We used the relaxed system as a starting configuration. As it is prior to system relaxation MD, energy minimization was carried out with a composite protocol of steepest descent using termination gradients of 100 kJ/mol·nm. The Nose´-Hoover thermostat [50]was used to maintain the equilibrium temperature at 298 K and periodic boundary conditions were imposed on all three dimensions. The Particle Mesh-Ewald method[51,52] was used to compute long-range electrostatics within a relative tolerance of 1×10^{-6}. A cut-off distance of 1nm was applied to real-space Ewald interactions. The same value was used for van der Waals interactions. The LINCS algorithm[53] was applied to constrain bond lengths of hydrogen atoms. A leap-frog algorithm[54] was used with a time step of 2 fs. The wave function were generated with the GFN-xTB method[55] using xtb 6.3 software. The structure of the input xtb software comes from the equilibrium state in the MD simulation. Calculation of reduced density gradient[42] and second largest eigenvalue of the electron density hessian (λ_2) were performed in Multiwfn 3.7 program[44]. The molecular structures can be visualized through visual molecular dynamics software (VMD, version 1.9.3)[56].

Data availability

The data that support the findings detailed in this study are available in the Article and its Supplementary Information or from the corresponding authors upon reasonable request.

References

1 Giri, N. *et al.* Liquids with permanent porosity. *Nature* **527**, 216-220, (2015).

2 Fulvio, P. F. & Dai, S. Porous liquids: the next frontier. *Chem* **6**, 3263-3287, (2020).

3 Jie, K., Zhou, Y., Ryan, H. P., Dai, S. & Nitschke, J. R. Engineering permanent porosity into liquids. *Advanced Materials* **33**, 2005745, (2021).

4 Ma, L. *et al.* Coordination cages as permanently porous ionic liquids. *Nature Chemistry* **12**, 270-275, (2020).

5 Zhang, J. *et al.* Porous liquids: a promising class of media for gas separation. *Angewandte Chemie International Edition* **54**, 932-936, (2015).

6 Gaillac, R. *et al.* Liquid metal–organic frameworks. *Nature Materials* **16**, 1149-11564, (2017).

7 Li, P. *et al.* Porous liquid zeolites: hydrogen bonding-stabilized H-ZSM-5 in branched ionic liquids. *Nanoscale* **11**, 1515-1519, (2019).

8 Li, P. *et al.* Electrostatic-assisted liquefaction of porous carbons. *Angewandte Chemie International Edition* **56**, 14958-14962, (2017).

9 Shan, W. *et al.* New class of type III porous liquids: a promising platform for rational adjustment of gas sorption behavior. *ACS Applied Materials & Interfaces* **10**, 32-36, (2018).

10 Shi, T. *et al.* Effect of pore size on the carbon dioxide adsorption behavior of porous liquids based on hollow silica. *ChemPhysChem* **19**, 130-137, (2018).

11 Kearsey, R. J., Alston, B. M., Briggs, M. E., Greenaway, R. L. & Cooper, A. I. Accelerated robotic discovery of type II porous liquids. *Chemical Science* **10**, 9454-9465, (2019).

12 Kumar, R., Dhasaiyan, P., Naveenkumar, P. M. & Sharma, K. P. A solvent-free porous liquid comprising hollow nanorod–polymer surfactant conjugates. *Nanoscale Advances* **1**, 4067-4075, (2019).

13 He, S. *et al.* General way to construct micro- and mesoporous metal–organic framework-based porous liquids. *Journal of the American Chemical Society* **141**, 19708-19714, (2019).

14 Egleston, B. D. *et al.* Controlling gas selectivity in molecular porous liquids by tuning the cage window size. *Angewandte Chemie International Edition* **59**, 7362-7366, (2020).

15 Cahir, J. *et al.* Type 3 porous liquids based on non-ionic liquid phases – a broad and tailorable platform of selective, fluid gas sorbents. *Chemical Science* **11**, 2077-2084, (2020).

16 Mow, R. E. *et al.* Colloidal three-dimensional covalent organic frameworks and their application as porous liquids. *Journal of Materials Chemistry A* **8**, 23455-23462, (2020).

17 Knebel, A. *et al.* Solution processable metal–organic frameworks for mixed matrix membranes using porous liquids. *Nature Materials* **19**, 1346-1353, (2020).

18 Deng, Z. *et al.* Facilitate gas transport through metal–organic polyhedra constructed porous liquid membrane. *Small* **16**, 1907016, (2020).

19 Lai, B. *et al.* Type 3 porous liquids for the separation of ethane and ethene. *ACS Applied Materials & Interfaces* **13**, 932-936, (2021).

20 Wang, D. *et al.* A universal approach to turn UiO-66 into type 1 porous liquids via post-synthetic modification with corona-canopy species for CO_2 capture. *Chemical Engineering Journal* **416**, 127625, (2021).

21 Hemming, E. B., Masters, A. F. & Maschmeyer, T. Exploring opportunities for platinum nanoparticles encapsulated in porous liquids as hydrogenation catalysts. *Chemistry – A European Journal* **26**, 7059-7064, (2020).

22 Cao, R. *et al.* Porous metal-organic framework liquids for enhanced CO_2 adsorption and catalytic conversion. *Angewandte Chemie International Edition* **60**, 20915-20920, (2021).

23 Bhattacharjee, A., Kumar, R. & Sharma, K. P. Composite porous liquid for recyclable sequestration, storage and in situ catalytic conversion of carbon dioxide at room temperature. *ChemSusChem* **14**, 3303-3314, (2021).

24 Giri, N. *et al.* Alkylated organic cages: from porous crystals to neat liquids. *Chemical Science* **3**, 2153-2157, (2012).

25 Melaugh, G., Giri, N., Davidson, C. E., James, S. L. & Pópolo, M. G. D. Designing and understanding permanent microporosity in liquids. *Physical Chemistry Chemical Physics* **16**, 9422-9431, (2014).

26 Jie, K. *et al.* Transforming porous organic cages into porous ionic liquids via a supramolecular complexation strategy. *Angewandte Chemie International Edition* **59**, 2268-2272, (2020).

27 Gosselin, A. J., Rowland, C. A. & Bloch, E. D. Permanently microporous metal–organic polyhedra. *Chemical Reviews* **120**, 8987-9014, (2020).

28 Iv, J. J. P., Perman, J. A. & Zaworotko, M. J. Design and synthesis of metal–organic frameworks using metal–organic polyhedra as supermolecular building blocks. *Chemical Society Reviews* **38**, 1400-1417, (2009).

29 Lee, S., Jeong, H., Nam, D., Lah, M. S. & Choe, W. The rise of metal–organic polyhedra. *Chemical Society Reviews* **50**, 528-555, (2021).

30 Desiraju, G. R. *Crystal engineering: the design of organic solids*. (Elsevier, Amsterdam, 1989).

31 Moulton, B. & Zaworotko, M. J. From molecules to crystal engineering: supramolecular isomerism and polymorphism in network solids. *Chemical Reviews* **101**, 1629-1658, (2001).

32 Zhang, D., Ronson, T. K., Zou, Y.-Q. & Nitschke, J. R. Metal–organic cages for molecular separations. *Nature Reviews Chemistry* **5**, 168-182, (2021).

33 Zhang, X. *et al.* Fine-tuning apertures of metal–organic cages: encapsulation of carbon dioxide in solution and solid state. *Journal of the American Chemical Society* **141**, 11621-11627, (2019).

34 Zhang, Z., Gao, W., Wojtas, L., Zhang, Z. & Zaworotko, M. J. A new family of anionic organic-inorganic hybrid doughnut-like nanostructures. *Chemical Communications* **51**, 9223-9226, (2015).

35 Murray, J., Kim, K., Ogoshi, T., Yao, W. & Gibb, B. C. The aqueous supramolecular chemistry of cucurbit[n]urils, pillar[n]arenes and deep-cavity cavitands. *Chemical Society Reviews* **46**, 2479-2496, (2017).

36 Wang, Y. *et al.* Cyclodextrin porous liquid materials for efficient chiral recognition and separation of nucleosides. *ACS Applied Materials & Interfaces* **12**, 45916-45928, (2020).

37 Brand, M. C. *et al.* Melt-quenched porous organic cage glasses. *Journal of Materials Chemistry A* **9**, 19807-19816, (2021).

38 Li, X. *et al.* Zeolitic imidazolate frameworks-based porous liquids with low viscosity for CO_2 and toluene uptakes. *Chemical Engineering Journal* **417**, 129239, (2021).

39 Greenaway, R. L. *et al.* Understanding gas capacity, guest selectivity, and diffusion in porous liquids. *Chemical Science* **8**, 2640-2651, (2017).

40 Asghar, M. A. *et al.* Reversible phase transition triggered by order–disorder transformation of carboxyl oxygen atoms coupled with distinct reorientations in $[HN(C_4H_9)_3](fumrate)_{0.5}\cdot(fumaric\ acid)_{0.5}$. *Crystal Growth & Design* **16**, 895-899, (2016).

41 Xu, Y., Zheng, Q. & Song, Y. Comparison studies of rheological and thermal behaviors of ionic liquids and nanoparticle ionic liquids. *Physical Chemistry Chemical Physics* **17**, 19815-19819, (2015).

42 Johnson, E. R. *et al.* Revealing noncovalent interactions. *Journal of the American Chemical Society* **132**, 6498-6506, (2010).

43 Jonckheere, D. *et al.* Adsorption and separation of aromatic amino acids from aqueous solutions using metal–organic frameworks. *ACS Applied Materials & Interfaces* **9**, 30064-30073, (2017).

44 Lu, T. & Chen, F. Multiwfn: a multifunctional wavefunction analyzer. *Journal of Computational Chemistry* **33**, 580-592, (2012).

45 Xiao, H. *et al.* Synergistic combination of the capillary effect of collagen fibers and size-sieving merits of metal–organic frameworks for emulsion separation with high flux. *Industrial & Engineering Chemistry Research* **59**, 14925-14934, (2020).

46 Li, X., Zhao, D. & Zheng, S. Recent advances in POM-organic frameworks and POM-organic polyhedra. *Coordination Chemistry Reviews* **397**, 220-240, (2019).

47 Christen, M. *et al.* The GROMOS software for biomolecular simulation: GROMOS05. *Journal of Computational Chemistry* **26**, 1719-1751, (2005).

48 Canzar, S. *et al.* Charge Group Partitioning in Biomolecular Simulation. *Journal of Computational Biology* **20**, 188-198, (2013).

49 Hess, B., Kutzner, C., van der Spoel, D. & Lindahl, E. GROMACS 4: Algorithms for highly efficient, load-balanced, and scalable molecular simulation. *Journal of Chemical Theory and Computation* **4**, 435-447, (2008).

50 Berendsen, H. J. C., Postma, J. P. M., van Gunsteren, W. F., DiNola, A. & Haak, J. R. Molecular dynamics with coupling to an external bath. *The Journal of Chemical Physics* **81**, 3684-3690, (1984).

51 Astrakas, L. G., Gousias, C. & Tzaphlidou, M. Structural destabilization of chignolin under the influence of oscillating electric fields. *Journal of Applied Physics* **111**, 074702, (2012).

52 Essmann, U. *et al.* A smooth particle mesh Ewald method. *The Journal of Chemical Physics* **103**, 8577-8593, (1995).

53 Hess, B., Bekker, H., Berendsen, H. J. C. & Fraaije, J. G. E. M. LINCS: A linear constraint solver for molecular simulations. *Journal of Computational Chemistry* **18**, 1463-1472, (1997).

54 Van Gunsteren, W. F. & Berendsen, H. J. C. A leap-frog algorithm for stochastic dynamics. *Molecular Simulation* **1**, 173-185, (1988).

55 Grimme, S., Bannwarth, C. & Shushkov, P. A robust and accurate tight-binding quantum chemical method for structures, vibrational frequencies, and noncovalent interactions of large molecular systems parametrized for all spd-block elements (z = 1–86). *Journal of Chemical Theory and Computation* **13**, 1989-2009, (2017).

56 Humphrey, W., Dalke, A. & Schulten, K. VMD: visual molecular dynamics. *Journal of Molecular Graphics* **14**, 33-38, (1996).

Declarations

Acknowledgements

We gratefully acknowledge the financial support from National Key R&D Program of China (2021YFE0191100), National Natural Science Foundation of China (21808104, 21676141), and Key R&D Program of Jiangsu Province (BE2021710).

Author contributions

Zhuxiu Zhang: Conceptualization, Investigation, Writing – original draft, Writing - review & editing. Baolin Yang: Simulation, Writing - original draft, Validation, Software, Visualization. Bingjie Zhang: Investigation, Methodology, Data analysis. Mifen Cui: Simulation, Data analysis, Validation. Jihai Tang: Supervision, Writing - review & editing. Xu Qiao: Project administration, Funding acquisition.

Competing interests

The authors declare no competing interests.

Figures

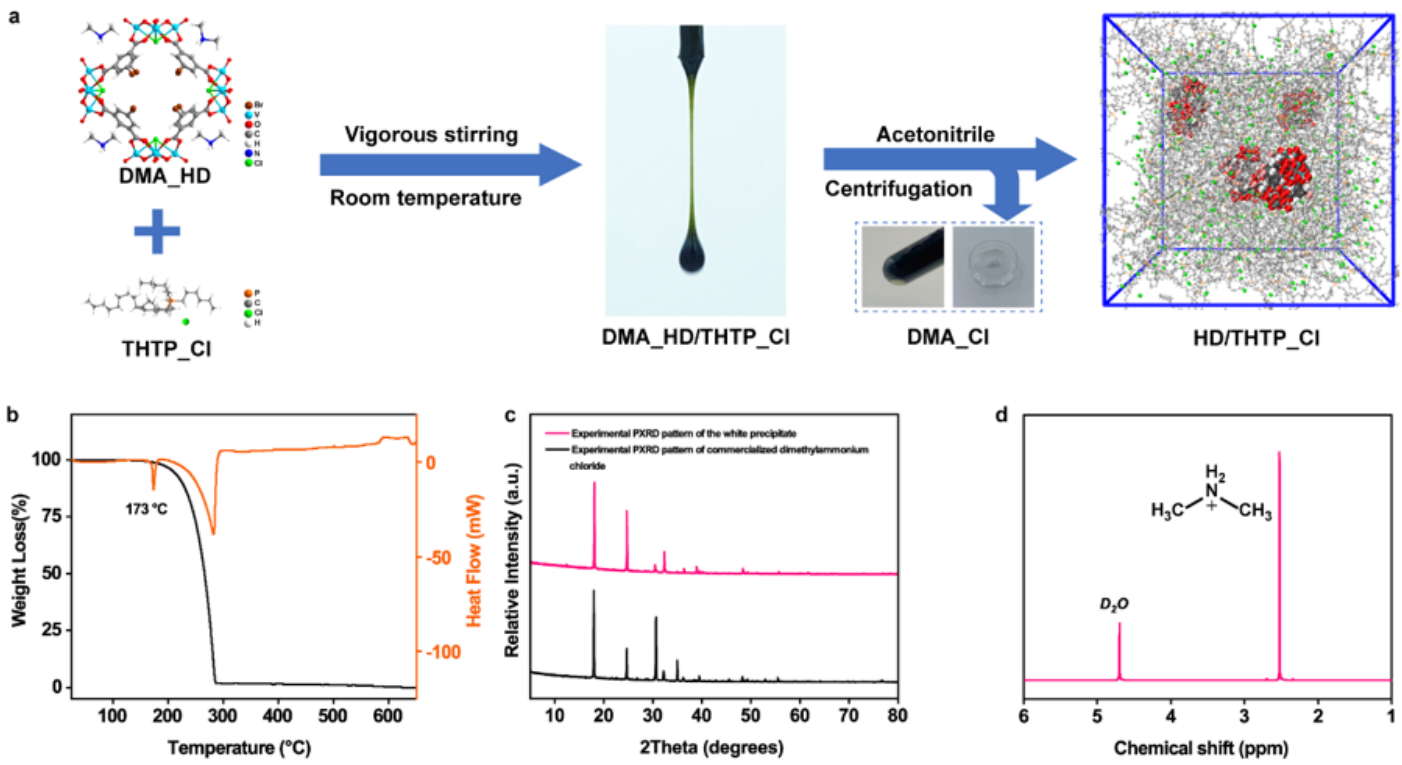

Figure 1

Synthesis of HD/THTP_Cl and characterization of the removed white precipitate characterization. a Schematic illustration of the synthesis of HD/THTP_Cl. b TG-DSC curve of the white precipitate. c Experimental PXRD pattern of the white precipitate and commercialized dimethylammonium chloride. d Partial 1H-NMR spectrum of the white precipitate.

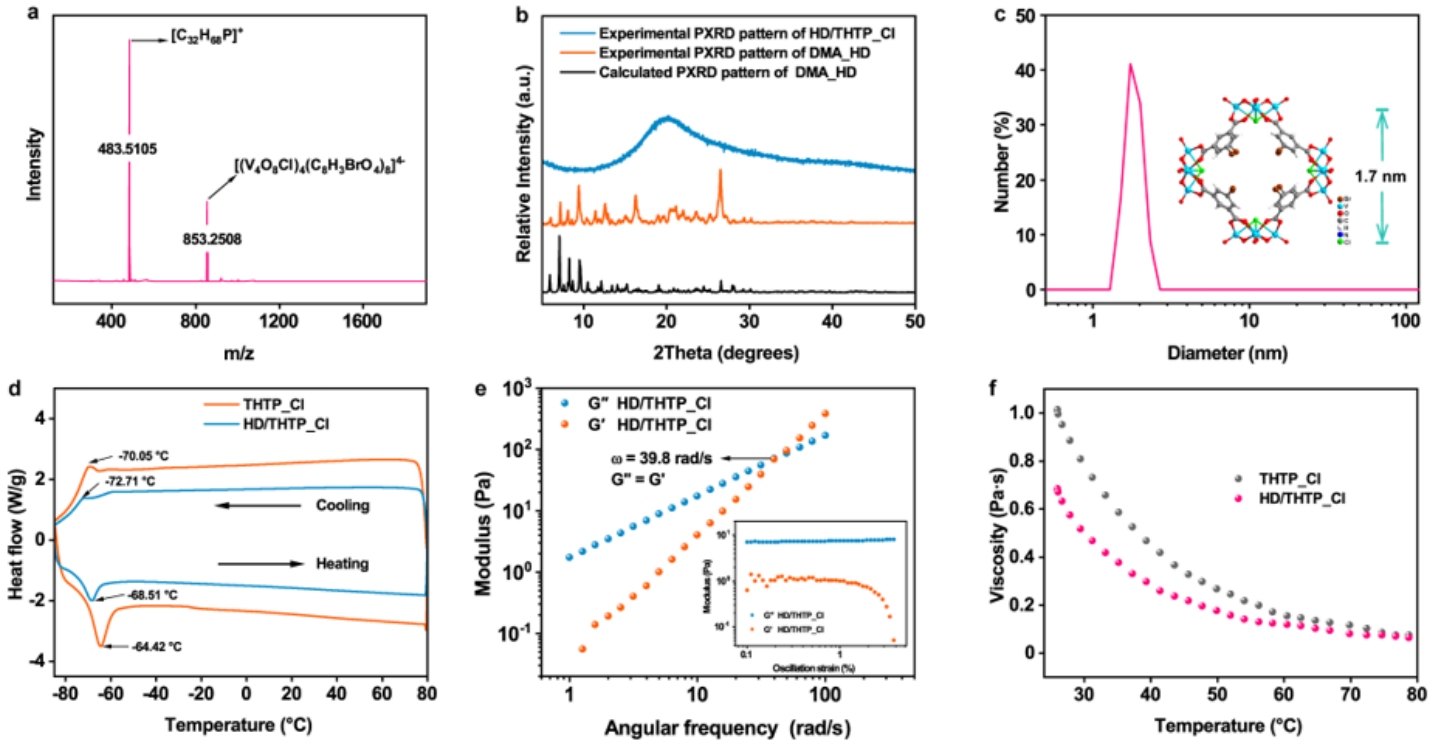

Figure 2

Structure characterizations of HD/THTP_Cl. a QTOF mass spectrum of HD/THTP_Cl. b Experimental PXRD patterns of DMA_HD and HD/THTP_Cl, and calculated PXRD pattern of DMA_HD. c Particle size and distribution from DLS measurements of HD/THTP_Cl in acetonitrile. Inset: Molecular structure of HD anion with the diameter of 1.7 nm. d DSC cooling and successive heating curves of THTP_Cl and HD/THTP_Cl. e Frequency-dependent modulus plots of HD/THTP_Cl. Inset: Strain-dependent modulus plots of HD/THTP_Cl with the angular frequency fixed at 5 rad/s. f Viscosity-temperature curves of THTP_Cl and HD/THTP_Cl.

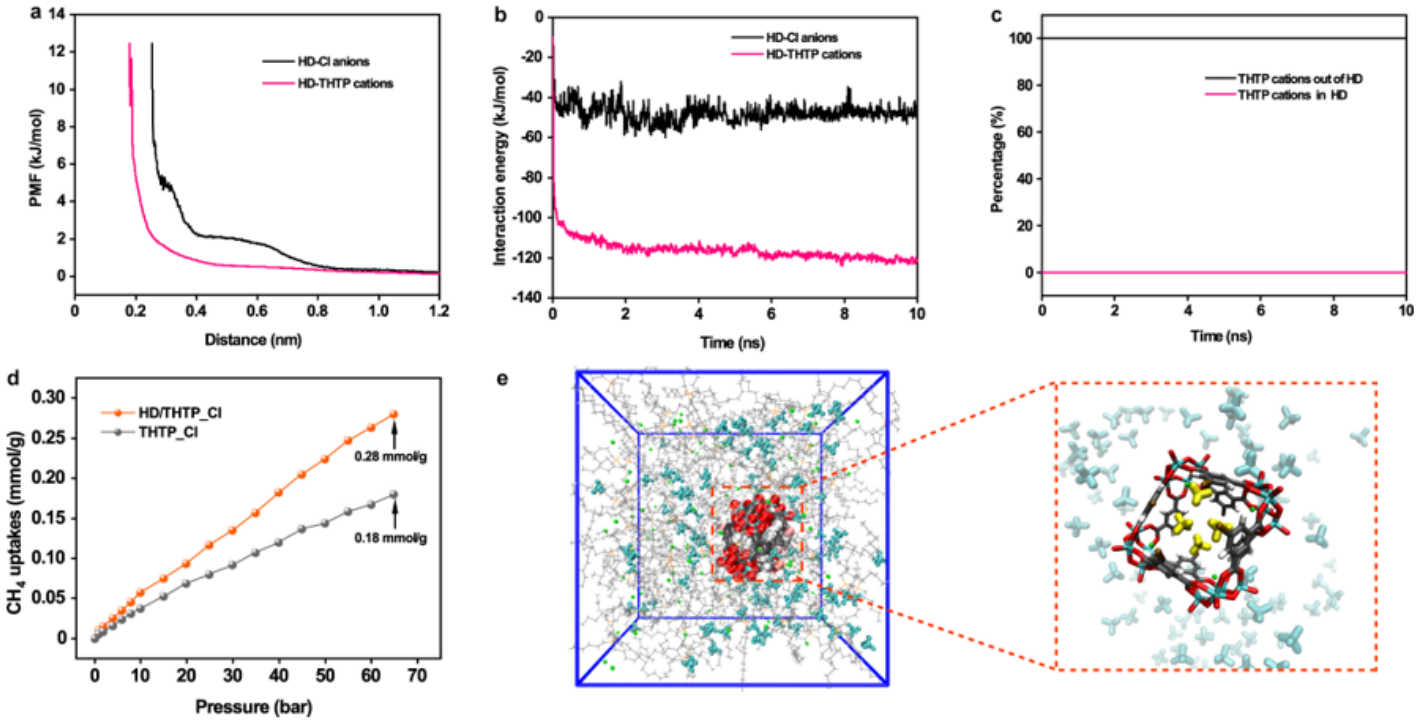

Figure 3

Porosity measurements. a Center-of-mass – a-particular-atom PMF for HD–THTP cations (P atom) and HD–Cl anions (Cl atom) from MD simulations. b The interaction energy of HD anion with THTP cation and chloride anion. c Simulated distribution percentage of THTP cation in and out of the cavity of HD. d High pressure CH4 adsorption isotherms of HD/THTP_Cl and THTP_Cl. e The simulation box of methane in HD/THTP_Cl at 25°C and 65 bar, in which the HD anion is occupied by four methane molecules. (Methane molecule inside and outside of HD are respectively highlighted with yellow and cyan.)

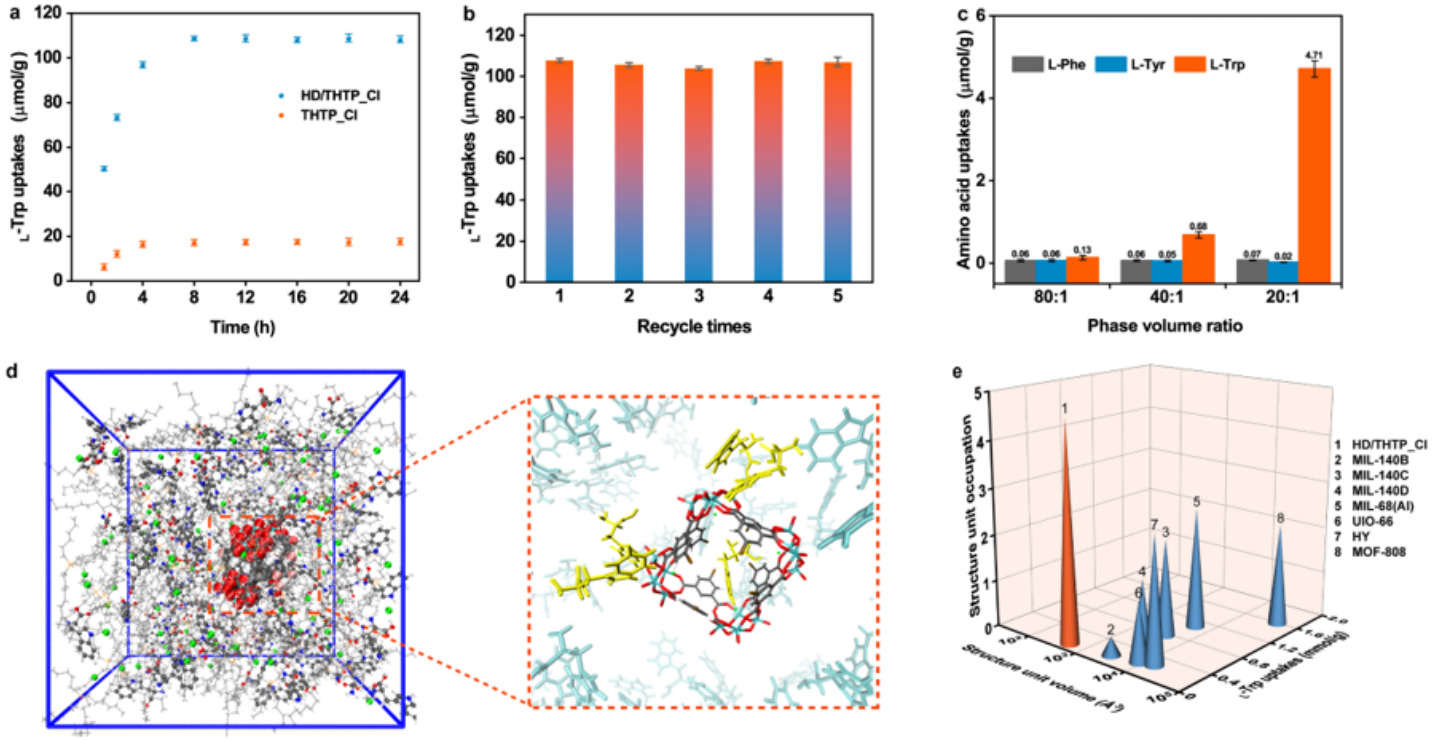

Figure 4

Selective extraction of L-Trp. a L-Trp uptake over time in HD/THTP_Cl and THTP_Cl. b The reuse of HD/THTP_Cl for the single-compound extraction of L-Trp. c Effect of the phase volume ratio on the L-Trp selectivity. d The simulation box of L-Trp in HD/THTP_Cl, in which the one molecule resides in the cavity of HD and four molecules interact with polyoxovanadates of HD. (The identified L-Trp molecule are respectively highlighted with yellow.) e Structure unit occupation of porous materials against structure unit volume and L-Trp uptakes.

Supplementary Files

This is a list of supplementary files associated with this preprint. Click to download.

- NCESI20211021.docx